Far-Field Drag Decomposition for Unsteady Flows.

H. Toubin, D. Bailly

▶ **To cite this version:**

H. Toubin, D. Bailly. Far-Field Drag Decomposition for Unsteady Flows.. 49th International Symposium of Applied Aerodynamics, Mar 2014, LILLE, France. hal-01059062

HAL Id: hal-01059062
https://onera.hal.science/hal-01059062

Submitted on 29 Aug 2014

HAL is a multi-disciplinary open access archive for the deposit and dissemination of scientific research documents, whether they are published or not. The documents may come from teaching and research institutions in France or abroad, or from public or private research centers.

L'archive ouverte pluridisciplinaire **HAL**, est destinée au dépôt et à la diffusion de documents scientifiques de niveau recherche, publiés ou non, émanant des établissements d'enseignement et de recherche français ou étrangers, des laboratoires publics ou privés.

La Société Savante de l'Aéronautique et de l'Espace

49th International Symposium of Applied Aerodynamics
Lille, 24-25-26 March 2014

FP30-2014-toubin

Far-Field Drag Decomposition for Unsteady Flows

Hélène Toubin [1], Didier Bailly [2]

[1] *Onera, The French Aerospace Lab, F92190 Meudon, France, Email: helene.toubin@onera.fr*
[2] *Onera, The French Aerospace Lab, F92190 Meudon, France, Email: didier.bailly@onera.fr*

ABSTRACT

Far-field decomposition methods are among the most powerful means to accurately compute the forces on an aircraft. They allow distinguishing between the drag components associated with the various physical phenomena: shock waves, viscous interactions and lift-induced vortex, without yet being fit to apply to unsteady configurations. Van der Vooren and Destarac have for example developed a powerful and reliable method used widely in the industry but restricted to steady flows. This paper presents a generalization to unsteady flows of this formulation. The demonstration relies on a strong theoretical background and allows the breakdown of drag into the three usual components only. This new unsteady formulation is applied to an OAT15A profile with buffeting, then to a NACA0012 profile at high angle of attack with natural vortex shedding. The results are analyzed and compared to the only other formulation available to break down the drag of unsteady flows.

1. INTRODUCTION

Recent drastic environmental and economic requirements such as ACARE in Europe lead the aeronautics actors to try to reduce as much as possible the aircraft consumption, and therefore the drag. Even a slight improvement on the drag can noticeably reduce the fuel consumption and the impact on the environment. In order to achieve these ambitious objectives, several ways can be chosen, such as aerodynamic optimization, control, or exploration of innovative designs. Among those designs, many involve complex unsteady phenomena, such as counter-rotating open rotors (CROR). In order to correctly quantify the gain of such breakthrough configurations, the drag must therefore be accurately computed for unsteady compressible flows.

Far-field drag computation was first introduced by Betz [1]. Instead of computing the forces on a body by integrating aerodynamic stresses on the skin (near-field methods), one can equivalently analyze the aerodynamic phenomena which occur within the fluid surrounding the body. This analysis is richer and allows distinguishing between the drag components associated with the various physical phenomena: shock waves, viscous interactions in the boundary layer and in the wake, and lift-induced vorticity. It can also identify a part of the spurious drag due to numerical dissipation. Onera has been working on far-field drag analysis for over a decade and has developed a reliable method for steady flows based on Van der Vooren's formulation [2]. However, no far-field method is for now able to successfully break down the drag of unsteady flows. Noca [3] has carried out an experimental study of several far-field formulations based on Wu equations [4]. Marongiu [5] as well as Xu [6] have applied similar methods to numerical unsteady flows, but like Noca, without achieving a physical breakdown. Gariépy [7] has also made a first attempt in generalizing Van der Vooren, but his decomposition still holds terms that cannot be matched with physical phenomena.

This paper presents a generalization of Van der Vooren's formulation to unsteady flows. It results in only viscous, wave, induced and spurious unsteady drag, and is valid for both URANS and DES simulations. This new unsteady formulation is analyzed and compared to Gariépy's formulation. Since Gariépy [8] uses Méheut's definition of an axial velocity defect [9], both expressions are first tested on steady cases to assess the reliability and accuracy of both approaches. The unsteady formulations are then applied to URANS computations: an OAT15A profile with buffeting, and a NACA0012 profile at high angle of attack with natural vortex shedding.

2. THEORY

The general equations which lead to the far-field breakdown of drag will be presented in this section. The steady formulation as introduced by Van der Vooren and Destarac [2] will first be redemonstrated in order to better understand the hypotheses which were made. The formulation will then be generalized to unsteady flows, before being compared to Gariépy's formulation.

2.1. General equations

The far-field theory consists in computing the aerodynamic force from the flow field analysis instead of the integration of the local stress on the body. The balance between the two approaches relies on the conservation of fluid momentum as described in Eq. 1. It requires no further assumption and is therefore valid for all unsteady compressible flows.

$$\int_V \frac{\partial \rho(\boldsymbol{q}-\boldsymbol{q}_\infty)}{\partial t}\mathrm{d}V = -\int_{\partial V} \rho(\boldsymbol{q}-\boldsymbol{q}_\infty)(\boldsymbol{q}.\boldsymbol{n})\,\mathrm{d}S - \int_{\partial V}(p-p_\infty)\boldsymbol{n}\,\mathrm{d}S + \int_{\partial V}(\boldsymbol{\tau}.\boldsymbol{n})\,\mathrm{d}S \quad (1)$$

The drag is obtained by taking the component along x and splitting the frontier of the domain ∂V into the body surface S_a and the outer surface S_e so as to get the near-field drag and the far-field drag on either side of the equation. The far-field drag can therefore be written as in Eq. 2, with $\boldsymbol{f} = -\rho(u-u_\infty)\boldsymbol{q} - (p-p_\infty)\boldsymbol{i} + \boldsymbol{\tau_x}$.

$$D_{ff} = \int_{S_e}(\boldsymbol{f}.\boldsymbol{n})\,\mathrm{d}S - \int_{S_a}\rho(u-u_\infty)(\boldsymbol{q}.\boldsymbol{n})\,\mathrm{d}S - \int_V \frac{\partial \rho(u-u_\infty)}{\partial t}\mathrm{d}V \quad (2)$$

The first surface term represents the flux of the physical sources of drag through the outer surface. The second surface term is due to the prospective motion of the body and will be zero in all the applications of this paper, and will therefore be dropped in the following equations. The volume term accounts for the time dependence as well as the propagation in time of the momentum.

2.2. Van der Vooren's formulation (steady)

For steady flows, the expression of the far-field drag reduces to the first surface integral in Eq. 2. Van der Vooren and Destarac's formulation consists in breaking down the expression of $\boldsymbol{f}$ into an irreversible and a reversible part.

They assume that a flow submitted to only irreversible processes is such that the pressure is equal to the reference pressure and the velocity parallel to the upstream velocity on a wake plane S_d sufficiently far from the drag sources.

This leads to the following decomposition, denoting u_{irr} the axial velocity on S_d under these assumptions:

$$\boldsymbol{f_{irr}} = -\rho(u_{irr}-u_\infty)\boldsymbol{q} + \boldsymbol{\tau_x} \quad (3)$$

The complementary is the reversible part:

$$\boldsymbol{f_{rev}} = -\rho(u-u_{irr})\boldsymbol{q} - (p-p_\infty)\boldsymbol{i} \quad (4)$$

We can then define the profile and induced drags as:

$$D_{vw} = \int_{S_d}(\boldsymbol{f_{irr}}.\boldsymbol{n})\,\mathrm{d}S \quad (5)$$

$$D_i = \int_{S_d}(\boldsymbol{f_{rev}}.\boldsymbol{n})\,\mathrm{d}S \quad (6)$$

The computation of u_{irr} given in Eq. 7 comes from thermodynamical considerations and the application of the irreversibility hypothesis.

$$u_{irr} = u_\infty\sqrt{1+\frac{2\Delta H}{u_\infty^2} - \frac{2}{(\gamma-1)M_\infty^2}\left(e^{\frac{\Delta s}{C_p}}-1\right)} \quad (7)$$

This definition holds only if $p_i \leq p_\infty$ as Méheut pointed out in his paper [9]. u_{irr} can therefore be undefined in regions where the flow is detached, where the vortices are strong, in the boundary layers if $M > M_\infty$ and downstream of strong shocks. However, the integration surfaces can be chosen around those regions, resulting in only quite small discrepancies.

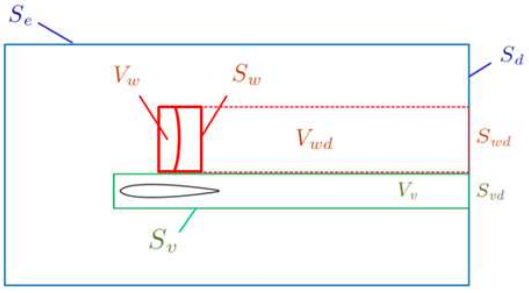

Figure 1. Volumes and surfaces used for the integrations

The profile drag can be further broken down into a wave and a viscous drag through a volume partition (see Fig. 1):

$$D_w = \int_{S_{wd}}(\boldsymbol{f_{irr}}.\boldsymbol{n})\,\mathrm{d}S \quad (8)$$

$$D_v = \int_{S_{vd}}(\boldsymbol{f_{irr}}.\boldsymbol{n})\,\mathrm{d}S \quad (9)$$

Since the flow is isentropic and steady downstream of the shock, the integration surface for the wave drag coefficient can be moved upstream and placed a little downstream of the shock.

The last step is to turn the wake integrals into closed surface integrals using the divergence theorem, in order to get a better numerical reliability. The spurious drag is then the difference between the near-field drag and the far-field drag. Eq. 10 summarizes the steady formulation.

$$\begin{aligned} D_w &= \int_{S_w} (\boldsymbol{f_{irr}}.\boldsymbol{n})\,\mathrm{d}S \\ D_v &= \int_{S_v} (\boldsymbol{f_{irr}}.\boldsymbol{n})\,\mathrm{d}S \\ D_i &= \int_{S_e} (\boldsymbol{f_{rev}}.\boldsymbol{n})\,\mathrm{d}S \\ D_{ff} &= D_w + D_v + D_i \\ D_{sp} &= D_{nf} - D_{ff} \end{aligned} \tag{10}$$

Note that a one vector formulation can be defined using the fact that $\boldsymbol{\nabla}.\boldsymbol{f} = 0$ everywhere.

2.3. Drag decomposition for unsteady flows

The extension to unsteady flows of the previous formulation is not as straightforward as it could seem. The approach presented here consists in computing the contribution of each isolated profile drag source.

2.3.1. Unsteady wave drag

Let us first consider an unsteady isolated shock wave. The drag created by this wave can be defined as the stress on the lateral surface of a streamtube enclosing the shock (see Fig. 1). The balance of momentum in this streamtube, neglecting the part upstream of the shock, gives the expression of the unsteady wave drag:

$$\begin{aligned} D_w = \int_{S_{wd}} -\rho(u_{irr}-u_\infty)(\boldsymbol{q}.\boldsymbol{n})\,\mathrm{d}S \\ -\int_{V_w+V_{wd}} \frac{\partial \rho(u-u_\infty)}{\partial t}\,\mathrm{d}V \end{aligned} \tag{11}$$

We can see that the whole flow information downstream of the shock is required in order to take into account the delay and the propagation of the source of drag. The wake surface integral can here also be moved closer upstream to the shock wave. However, because of the unsteadiness of the flow, new terms arise from this transformation.

Eq. 12 is the result of several manipulations using the divergence theorem.

$$\begin{aligned} D_w = \int_{S_w} -\rho(u_{irr}-u_\infty)(\boldsymbol{q}.\boldsymbol{n})\,\mathrm{d}S \\ -\int_{V_w} \frac{\partial \rho(u-u_\infty)}{\partial t}\,\mathrm{d}V \\ -\int_{V_{wd}} \left(\frac{\partial \rho(u-u_{irr})}{\partial t} + \frac{1}{u_{irr}}\frac{\partial p}{\partial t}\right)\mathrm{d}V \end{aligned} \tag{12}$$

The point of this manipulation is that the last volume integral is small compared to the others (around 5% of the wave drag), so that the numerical errors are reduced.

2.3.2. Unsteady viscous drag

We now consider an isolated profile in an unsteady flow, without shock waves. We are still working in a streamtube around the profile, neglecting the upstream part. The time derivative term also adds to the steady one:

$$\begin{aligned} D_v = \int_{S_v} (-\rho(u_{irr}-u_\infty)\boldsymbol{q} + \boldsymbol{\tau_x}).\boldsymbol{n}\,\mathrm{d}S \\ -\int_{V_v} \frac{\partial \rho(u-u_\infty)}{\partial t}\,\mathrm{d}V \end{aligned} \tag{13}$$

One could also do a similar manipulation as in the shock wave case to integrate closer to the profile but it was not judged necessary here since the wake volume integral would remain large.

2.3.3. Unsteady induced drag

The induced drag is the complementary part of the total drag:

$$\begin{aligned} D_i = \int_{S_e} (-\rho(u-u_{irr})\boldsymbol{q} - (p-p_\infty)\boldsymbol{i}).\boldsymbol{n}\,\mathrm{d}S \\ +\int_{S_d\setminus(S_{wd}+S_{vd})} -\rho(u_{irr}-u_\infty)(\boldsymbol{q}.\boldsymbol{n})\,\mathrm{d}S \\ -\int_{V\setminus(V_w+V_{wd}+V_v)} \frac{\partial \rho(u-u_\infty)}{\partial t}\,\mathrm{d}V \end{aligned} \tag{14}$$

Let us call $V_d = V\setminus(V_w + V_{wd} + V_v)$. The second wake surface integral can be moved similarly to the shock wave case, giving the same terms in the volume V_d:

$$\begin{aligned} D_i = \int_{S_e} (-\rho(u-u_{irr})\boldsymbol{q} - (p-p_\infty)\boldsymbol{i}).\boldsymbol{n}\,\mathrm{d}S \\ -\int_{V_d} \left(\frac{\partial \rho(u-u_{irr})}{\partial t} + \frac{1}{u_{irr}}\frac{\partial p}{\partial t}\right)\mathrm{d}V \end{aligned} \tag{15}$$

If the fluid is inviscid without any shock, then V_d becomes the whole volume and therefore the induced drag gives the total drag as expected. This expression is however not completely satisfactory because the volume term can contain irreversible phenomena such as viscous terms

which propagated in the fluid domain. A validation in Euler, RANS, 2D and 3D test cases is required before applying it to complex cases.

2.3.4. Final decomposition

The final decomposition is given in Eq. 16:

$$
\begin{aligned}
D_w &= \int_{S_w} (\boldsymbol{f_{irr}}.\boldsymbol{n})\,\mathrm{d}S - \int_{V_w} \frac{\partial \rho(u-u_\infty)}{\partial t}\mathrm{d}V \\
&\quad - \int_{V_{wd}} \left(\frac{\partial \rho(u-u_{irr})}{\partial t} + \frac{1}{u_{irr}}\frac{\partial p}{\partial t} \right) \mathrm{d}V \\
D_v &= \int_{S_v} (\boldsymbol{f_{irr}}.\boldsymbol{n})\,\mathrm{d}S - \int_{V_v} \frac{\partial \rho(u-u_\infty)}{\partial t}\mathrm{d}V \\
D_i &= \int_{S_e} (\boldsymbol{f_{rev}}.\boldsymbol{n})\,\mathrm{d}S \\
&\quad - \int_{V_d} \left(\frac{\partial \rho(u-u_{irr})}{\partial t} + \frac{1}{u_{irr}}\frac{\partial p}{\partial t} \right) \mathrm{d}V \\
D_{ff} &= D_w + D_v + D_i \\
D_{sp} &= D_{nf} - D_{ff}
\end{aligned}
\tag{16}
$$

Some remarks can be made at this point:

- The steady formulation is retrieved when the time-derivative terms are removed.
- The zones where u_{irr} is undefined are usually concentrated in V_w and V_v so that it can be used in most cases. However another decomposition of the axial velocity developed by Méheut [9] is available for more complex cases (see section 2.4.1.).

2.4. Gariépy decomposition

Let us now compare our formulation with that of Gariépy [7]. His formulation is the first attempt in breaking down the unsteady drag. He uses the definition of the axial velocity defect first introduced by Méheut [9].

2.4.1. A new expression for the axial velocity

Méheut [9] tackles the decomposition of the axial velocity the other way around: he assumes that the flow is reversible (entropy and enthalpy are constant) on a wake plane S'_d. It gives a reversible velocity:

$$
u_{rev} = u_\infty \sqrt{1 - \frac{2}{(\gamma-1)M_\infty^2}\left(\left(\frac{p}{p_\infty}\right)^{\frac{\gamma-1}{\gamma}} - 1 \right) - \frac{v^2+w^2}{u_\infty^2}}
\tag{17}
$$

Remember that we needed to move the wake integration surface upstream to compute the wave drag, using the isentropy of the flow. Now the velocity that we want to move is $u - u_{rev}$. It depends only on Δs and ΔH in a first approximation. It is therefore expected that the closer we integrate from the source of drag, the less reliable this expression is.

Gariépy also assesses in his paper [8] that ΔH should be added to the expression of u_{rev} when computing the profile drag. The superscript * will be added to the corresponding expressions:

$$
u^*_{rev} = u_\infty \sqrt{1 - \frac{2}{(\gamma-1)M_\infty^2}\left(\left(\frac{p}{p_\infty}\right)^{\frac{\gamma-1}{\gamma}} - 1 \right) - \frac{v^2+w^2}{u_\infty^2} + \frac{2\Delta H}{u_\infty^2}}
\tag{18}
$$

It is equivalent to removing ΔH from u_{irr}. If it is of small consequences in steady cases (a few drag counts at most), the effect is much stronger for unsteady cases since the enthalpy varies strongly in time. Our opinion is that the enthalpy due to the unsteadiness of a shock should appear inside the wave drag. Same goes for the viscous drag.

A study in steady flow case will be carried out in section 3.1. to confirm these allegations.

2.4.2. Gariépy unsteady decomposition

Gariépy [7] introduces the former expression of the axial velocity defect within the steady decomposition. He suggests including the time-derivative terms into an unsteady drag coefficient. He also defines a spurious drag from the integration of terms he judges small outside the zones of production of drag. His formulation can be written as follows:

$$
\begin{aligned}
D_w^G &= \int_{S_w} (\boldsymbol{f^*_{irr}}.\boldsymbol{n})\,\mathrm{d}S \\
D_v^G &= \int_{S_v} (\boldsymbol{f^*_{irr}}.\boldsymbol{n})\,\mathrm{d}S \\
D_i^G &= \int_{S_e} (\boldsymbol{f_{rev}}.\boldsymbol{n})\,\mathrm{d}S \\
D_{uns}^G &= \int_{S_e} (\boldsymbol{f^*_{rev}} - \boldsymbol{f_{rev}}).\boldsymbol{n}\,\mathrm{d}S \\
&\quad - \int_V \frac{\partial \rho(u-u_\infty)}{\partial t}\mathrm{d}V \\
D_{sp}^G &= \int_{V_{wd}+V_d} (\boldsymbol{\nabla}.\boldsymbol{f^*_{irr}})\,\mathrm{d}V \\
D_{ff}^G &= D_w^G + D_v^G + D_i^G + D_{uns}^G + D_{sp}^G
\end{aligned}
\tag{19}
$$

Here are some remarks about this formulation:

- Gariépy deliberately chose to assign all unsteady phenomena to an unsteady drag coefficient.
- The use of the axial velocity u^*_{rev} is questionable as noted in 2.4.1.

- The wave drag coefficient does not take into account the wake of the shock and therefore the delay and propagation of the variations in time. One can expect that a variation of the extension of the integration surface downstream of the shock will lead to strong variations in this drag coefficient.
- Gariépy assets in his paper that $\nabla . f^*_{irr}$ is located only in the regions of production of drag (shocks, boundary layers and wakes). However the irreversible terms can propagate in the rest of the domain, so that the spurious drag thus defined can be very strong. The calculations performed in this study have confirmed this observation.

Both unsteady formulations have been implemented and are compared in section 3.

3. APPLICATIONS

The formulations are first applied to steady test cases. They are then tested on two unsteady configurations which allow drawing some conclusions about the validity of the approach. The Onera code *elsA* is used for every computation. Jameson numerical scheme is used and the turbulence model chosen is Spalart-Allmaras except for the last unsteady case. The unsteady computations are URANS calculations.

3.1. Comparative study on steady flows

The different expressions available for the computation of the axial velocity defect have been compared in many steady cases, Euler, RANS, 2D and 3D, with or without angle of attack. The downstream extension of the integration surfaces varies during the study. The aim is to check the validity of the use of u_{rev} and u^*_{rev} compared to u_{irr} as we change the integration domain. All cases gave the same conclusions, which we can summarize with a general case of a 3D wing in a transonic flow with a non zero angle of attack.

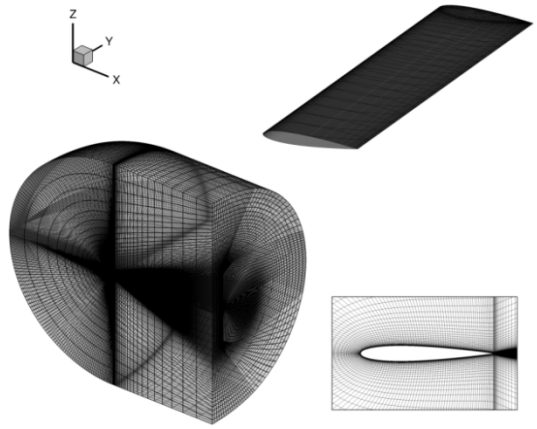

Figure 2. Visualization of the mesh of the rectangular NACA0012-based wing

The wing is a rectangular NACA0012-based wing. The mesh is around 1 million nodes and is shown in Fig. 2. The aerodynamic conditions are: $M_\infty = 0.8$, $\alpha = 2.5°$ and $Re = 3.10^6$.

The convergence curves shown in Fig. 3 show that the computation is very well converged after the 10,000 iterations. The variation of the near-field drag coefficient (in blue) in particular is less than a thousandth of drag count.

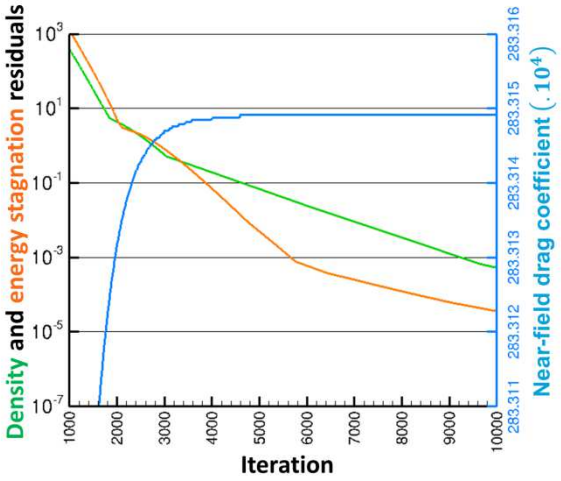

Figure 3. Convergence curves of the steady 3D test case

The flow field is presented in Fig. 4. The shock wave on the upper side is quite strong and a vortex appears at the tip of the wing.

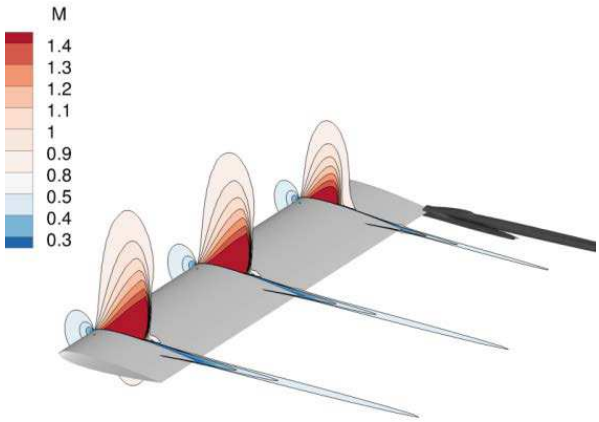

Figure 4. Mach contours and iso-surface of vorticity

The flow field is post-processed after 10,000 iterations by the in-house code *ffd72*. The first step of far-field drag extraction is the definition of the integration surfaces using volume criteria. Those criteria are described in [2]. The downstream extension of the integration surfaces

can vary at the demand of the user. Fig. 5 shows an example of the integration surfaces for a given downstream extension.

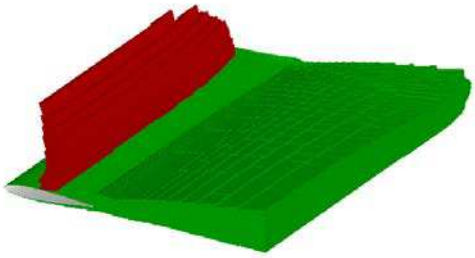

Figure 5. Integration surfaces for the steady 3D test case (red = shock, green = viscous)

Once the surfaces defined, the drag coefficients are computed by *ffd72*. The downstream extension of the surfaces was set to vary in Fig. 6, allowing a comparison between the three expressions of the axial velocity defect. The classical expression using u_{irr} as defined by Van der Vooren and Destarac is quite reliable, even very close to the sources of drag. The expressions with u_{rev} and u^*_{rev} give less satisfactory results. These observations are consistent with the theoretical remarks made in sections 2.2. and 2.4.1. Another comment is that there is very small difference between u_{rev} and u^*_{rev} in the steady case. It will not be the case for unsteady applications.

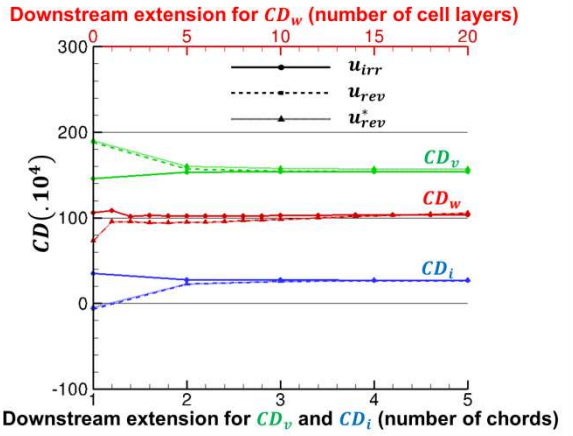

Figure 6. Evolution of the wave, viscous and induced drag with respect to the downstream extension of the integration surfaces

The conclusion of this first study is that the integration surfaces must be chosen very carefully. We will also try to use as much as possible u_{irr} instead of u_{rev} in the future applications.

3.2. Buffeting

The first unsteady test case is an OAT15A profile under buffeting conditions. The mesh is 2D with around 300,000 nodes (see Fig. 7).

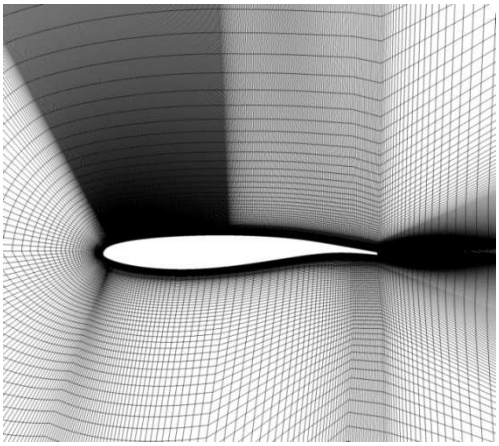

Figure 7. Visualization of the mesh of the OAT15A profile

The study was carried out over one period, with a time step of 2.10^{-5}, which corresponds to 1,000 steps by period. The Mach number is $M_\infty = 0.2$, $\alpha = 4.5°$ and $Re = 13.10^6$. The unsteady computation was converged over several periods in order to reach the full periodicity and avoid the transient phenomena. The curve of lift vs drag over one period is then perfectly closed.

Fig. 8 shows the instantaneous flow field taken when the shock is in the downstream position at iteration 500.

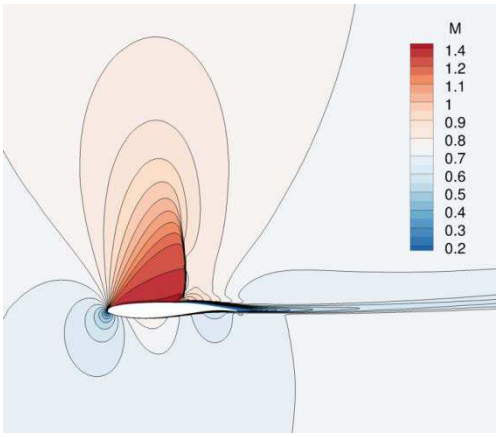

Figure 8. Mach contours of the buffeting case at iteration 500

The integration surfaces computed by *ffd72* at the same iteration are shown in Fig. 9. Recall that the integration surface for the induced drag is the outer surface, and V_d is the complementary volume of the volumes shown in Fig. 9 in the whole control volume.

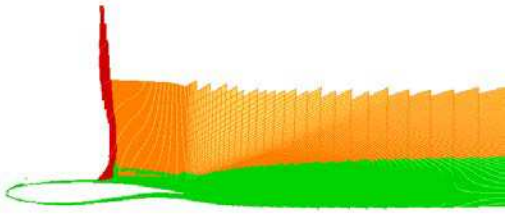

Figure 9. Integration surfaces for the buffeting case (red = shock, orange = shock wake, green = viscous) at iteration 500

The drag extraction was carried out over one period. The resulting time evolutions are shown in Fig. 10. The formulation developed and described in this paper is in solid lines. The total far-field drag (pink) increases while the shock moves downstream and decreases while the shock moves upstream. It is in good agreement with the near-field drag. The spurious drag (orange) is indeed at most 20 drag counts or 2% of the total drag.

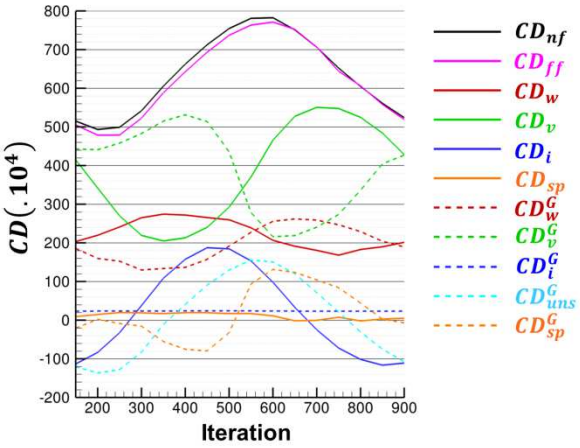

Figure 10. Evolution of the drag coefficients with respect to time over one period of the buffeting configuration

The validation of the other drag coefficients can only be qualitative by analyzing the flow field. The components will also be compared to those obtained using Gariépy's formulation.

The wave drag (red) takes values between 170 and 280 drag counts. It is strongest when the shock is at the most downstream position, as expected. The viscous drag (green) varies between 200 and 550 drag counts. It is strongest when the shock is close to the leading edge and the flow separation is the strongest. The time evolution seems therefore valid. What is noticeable is the strong induced drag (blue) which oscillates between negative and positive values. The induced drag is zero for steady 2D configurations. For unsteady cases however, the vorticity is continuously shed in the wake, leading to variations in the lift and therefore in the induced drag, which might explain the evolution observed.

Gariépy's formulation results are presented in dashed lines, with the same colors. It was found that the choice of the integration surfaces, in particular the downstream extension of the viscous volume, had a very strong impact on the results. The downstream extension was chosen of 3 chords in order to get the least spurious drag. The far-field drag is equal to the former one since only the decomposition is different. The wave and viscous drag coefficients are in phase opposition, so that they mismatch the physical phenomena. The induced drag is quite small and constant in time. The unsteady drag coefficient (light blue) on the contrary is strong with positive and negative values. It is remarkable that this unsteady coefficient is rather close to the induced coefficient computed with the new formulation. The induced drag is indeed mainly due to the unsteadiness. The spurious drag is rather strong, at most 12% of the total drag.

The conclusion of this first test case is that the unsteady formulation gives good results but requires further validation regarding the induced drag expression.

3.3. Vortex shedding

The second unsteady case is the natural vortex shedding downstream of a NACA0012 profile at $\alpha = 20°$ at low Mach number $M_\infty = 0.2$ and $Re = 2.10^6$. The turbulence model is here $k - \omega$ and the numerical scheme is AUSM-P. The far-field drag reduces to viscous and induced drags, allowing a better understanding of the decomposition.

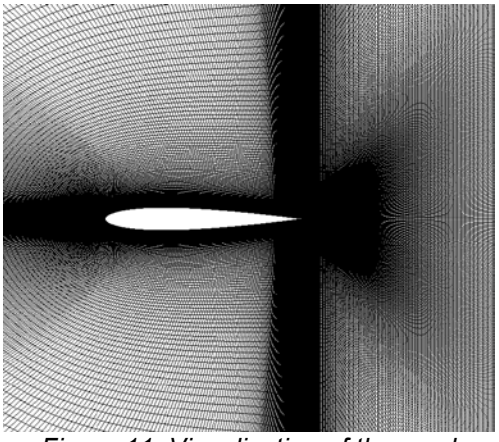

Figure 11. Visualization of the mesh of the NACA0012 profile

The mesh is a 550,000 nodes 2D mesh (see Fig. 11). The time step is 5.10^{-6}, which corresponds to 3,000 steps by period. Here again several periods were simulated before extracting the flow field and the periodic state was ensured looking at lift vs drag curves.

The flow field is presented in Fig. 12. Two vortices are emitted periodically starting from the leading edge. They are then advected along the wake.

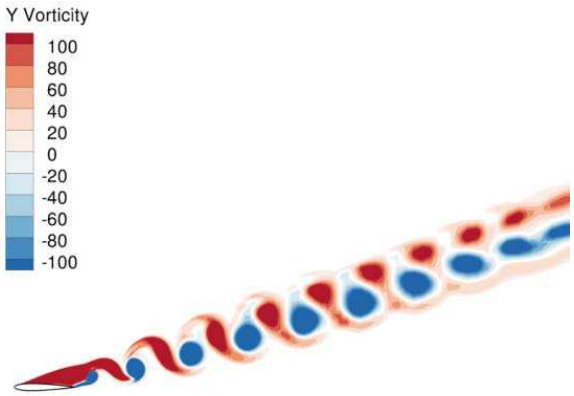

Figure 12. Vorticity contours of the vortex shedding case at iteration 2000

The integration volumes are computed at each extraction of drag. An example of the viscous volume is shown in Fig. 13. The induced surface is there again the outer surface and the complementary volume is the complementary of the viscous volume.

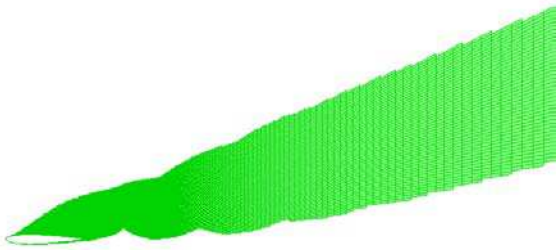

Figure 13. Viscous integration surface for the vortex shedding case at iteration 2000

The drag extraction is carried out over one period. The resulting time evolution curves are shown in Fig. 14. The far-field drag (pink) is in good agreement with the near-field drag (black). Their peaks match the instant when a pair of vortices is released. The high level of drag is consistent with the experimental results of Mesquita [10].

The results of the new formulation are presented in solid lines. The viscous drag (green) is the strongest when the separation occurs. The induced drag (blue) is here also non zero. However in this case it remains positive with relatively small values. Its variations are consistent with the variations of vorticity which is created at the separation instant. We could have expected it to vary in negative and positive values as in the previous test case. It is difficult to find a correct explanation since the wake is very wide, resulting in a non obvious split of the viscous and induced drags. The spurious drag (orange) is rather small, around 1% of the total drag.

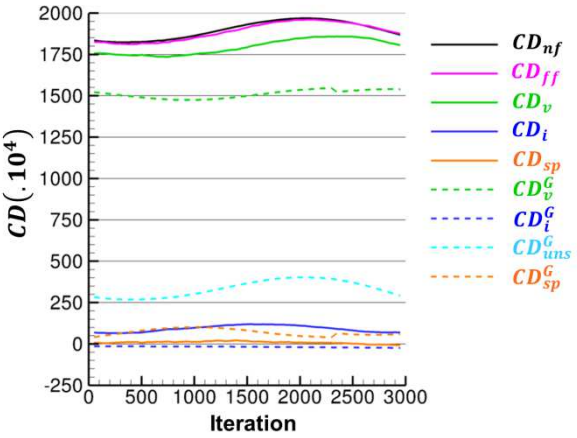

Figure 14. Evolution of the drag coefficients with respect to time over one period of the vortex shedding configuration

Gariépy's formulation is presented in dashed lines. The volumes were also chosen so as to get the least spurious drag. It is however stronger, at most 100 drag counts or 5% of the total drag. The unsteady drag term is also quite strong. The induced drag is almost zero and negative and the viscous drag is under estimated compared to the other formulation.

This second test case therefore confirms the first one: the new formulation gives satisfactory drag coefficient evolutions even though the induced drag coefficient requires further investigations.

4. CONCLUSION

Van der Vooren's far-field drag breakdown method has been extended to unsteady flows. The new formulation includes unsteady terms into each drag coefficient rather than gathering them in an unsteady drag coefficient. Since Van der Vooren's definition of the axial velocity defect is not always defined, a new expression introduced by Méheut and used by Gariépy is described and

compared in various steady configurations. The results show that it is not as reliable as Van der Vooren's definition and should be used with caution.

A theoretical analysis of Gariépy's formulation also reveals weaknesses that we have tried to revise. Both unsteady formulations were tested on two URANS configurations: a 2D buffeting case and a 2D vortex shedding case. The applications confirm what the theoretical analysis had predicted: although we still lack understanding for the induced drag, the suggested decomposition gives good results. We get little spurious drag and modifications in the integration domains do not alter or put the coefficients out of phase, unlike Gariépy's.

Further work will deal with validating the breakdown between viscous and induced drags. Oscillating profiles and wings, in Euler or RANS computations will be carried out. More complex URANS and DES test cases will then be considered, such as buffeting or spoilers. A CROR test case should be the following application, aiming to the quantification of the true efficiency of such breakthrough engines. Vorticity-based formulations will also be investigated, since they are likely better suited to unsteady flows.

ACKNOWLEDGMENTS

The authors thank their colleagues from the Applied Aerodynamics Department M. Costes for his expertise on vorticity and moving bodies, and D. Destarac for his support and great experience in far-field drag extraction.

REFERENCES

1. Betz, A. (1925).
A Method for the Direct Determination of Wing-Section Drag. Tech. rep., *ZFM.*

2. Van der Vooren, J. & Destarac, D. (2004).
Drag/Thrust Analysis of a Jet-propelled Transonic Transport Aircraft: Definition of Physical Drag Components. *Aerospace Science and Technology*, **8**, 545-556.

3. Noca, F. (1997).
On the evaluation of Time-Dependent Fluid-Dynamic Forces on Bluff Bodies. Ph.D. thesis, California Institute of Technology.

4. Wu, J.-Z., Ma H.-Y. & Zhou, M.-D. (2006). *Vorticity and Vortex Dynamics.* Springer.

5. Marongiu, C. & Tognaccini, R. (2010).
Far-Field Analysis of the Aerodynamic Force by Lamb Vector Integrals. *AIAA Journal*, **48**(11), 2543-2555.

6. Xu, C.-Y., Chen, L.-W. & Lu, X.-Y. (2010).
Large-Eddy Simulation of the Compressible Flow past a Wavy Cylinder. *Journal of Fluid Mechanics*, **664**, 238-273.

7. Gariépy, M., Trépanier, J.-Y. & Malouin, B. (2013).
Generalization of the Far-Field Drag Decomposition Method to Unsteady Flows. *AIAA Journal*, **51**(6), 1309-1319.

8. Gariépy, M. & Trépanier, J.-Y. (2011).
A New Far-Field Drag Decomposition Formulation Relevant to Highly Seperated Flows. In Proc. CASI AERO Conference, Montréal, Canada.

9. Méheut, M. & Bailly, D. (2008).
Drag-Breakdown Methods from Wake Measurements. *AIAA Journal*, **46**(4), 847-862.

10. Mesquita, A.-L.-A. (2001).
Experimental Analysis of Airfoil for High Angle of Attack. *Revista Virtual de Iniciao Acadmica da UFPA*, **1**(2).